metals

MDPI

Article

Effect of Laser Welding Parameters with Different Fillers on Solidification Cracking and Mechanical Properties of AA7075

Mohammed Alkhabbat [1], François Nadeau [2], Fatemeh Mirakhorli [2], Thien-My Dao [1] and Xuan-Tan Pham [1,*]

[1] École de Technologie Supérieure, Montréal, QC H3C 1K3, Canada; mohammed.alkhabbat.1@ens.etsmtl.ca (M.A.); thien-my.dao@etsmtl.ca (T.-M.D.)
[2] National Research Council of Canada, Saguenay, QC G7H 8C3, Canada; francois.nadeau@nrc.ca (F.N.); fatemeh.mirakhorli@cnrc-nrc.gc.ca (F.M.)
* Correspondence: tan.pham@etsmtl.ca

Abstract: AA7075 is considered a 'non-weldable' alloy using fusion welding methods. In this study, laser welding is applied in pulse mode to weld 2 mm thick AA7075 aluminum alloy plates using different fillers. The aim is to identify the influence of welding parameters and fillers on solidification cracking susceptibility during laser welding using the circular patch test (CPT). X-ray radiography was used to detect and measure cracks in the CPT samples. Furthermore, the effects of the laser welding process and chemical composition of fillers on the accumulated crack length (CCL), microstructure, and mechanical properties were investigated. Moreover, the mechanical behavior and local deformation of the fusion zone (FZ) were investigated using micro-flat tensile tests with digital image correlation. The mechanical properties of the FZ were correlated with the CCL as well as with the microstructure of the FZ, which was investigated experimentally. The results show that the chemical composition of fillers and welding speed affect the CCL of solidification cracks. Changes in the microstructure were observed within the fusion zone, and the structure became uniform and finer with the formation of Mg_2Si and magnesium-rich, copper, and zinc (η-phase) particles.

Keywords: solidification cracks; AA7075 aluminum alloy; laser welding; accumulated crack length

check for updates

Citation: Alkhabbat, M.; Nadeau, F.; Mirakhorli, F.; Dao, T.-M.; Pham, X.-T. Effect of Laser Welding Parameters with Different Fillers on Solidification Cracking and Mechanical Properties of AA7075. *Metals* **2023**, *13*, 1704. https://doi.org/10.3390/met13101704

Academic Editor: Yanxi Zhang

Received: 30 August 2023
Revised: 25 September 2023
Accepted: 3 October 2023
Published: 7 October 2023

Copyright: © 2023 by the authors. Licensee MDPI, Basel, Switzerland. This article is an open access article distributed under the terms and conditions of the Creative Commons Attribution (CC BY) license (https://creativecommons.org/licenses/by/4.0/).

1. Introduction

Laser welding technology, when used on aluminum alloys, has significant potential as a joining method due to its high productivity, low heat input, small weld bead, narrow heat-affected zone (HAZ), and slighter thermal distortion compared to other welding processes [1–3]. Laser welding is highly influenced by the physical properties of welded aluminum [4]. Aluminum alloys have certain intrinsic properties, such as the tendency to form low-fusion components and low laser beam absorption [5–7]. A variety of defects, such as porosities and solidification cracking, can thus be formed during the laser welding of Al alloys [8,9]. However, the laser welding of high-strength AA7075 aluminum alloys has not been comprehensively investigated due to their poor weldability characteristics for fusion welding techniques such as solidification cracking and softening in the HAZ and fusion zone (FZ). The properties of AA7075 are intricately linked to its evolving structure during formation, which particularly affects the strength and plasticity of the α-phase. This primary phase comprises aluminum as its base with various alloying elements, including Zn, Mg, and Cu. Additionally, the arrangement of eutectic silicon and Fe-containing phases, which emerge during the eutectic and secondary crystallization of melts, profoundly influence the alloy's mechanical characteristics. Furthermore, intermetallic phases, common in aluminum alloys, exert a significant influence on the material's properties in AA7075. The key secondary phases encountered in AA7075 encompass the η-phase ($MgZn_2$), Al_2CuMg, $Al_2Mg_3Zn_3$, and Al_2Cu. Their geometry, dimensions, density, and distribution have a direct impact on both their mechanical properties and susceptibility to solidification cracking [7,10,11].

AA7075 has a significant solidification cracking tendency due to low-melting-point alloying elements such as Mg and Zn, the high coefficient of thermal expansion, and the large solidification shrinkage [12–14]. Several works have examined the reasons underlying the emergence of cracking during laser welding. It was found that solidification cracking mostly occurs due to the segregation of alloying elements at grain boundaries and the existence of low-melting-point phases [15–17]. Zhao et al. [15] investigated the initiation of solidification cracking by studying the effect of a mass fraction of Si content in Al-Mn-Mg aluminum alloys during laser welding. The results suggested that solidification cracking will form if there is a significant amount of low-melting-point eutectic liquid phases as films at grain boundaries during solidification after laser welding, which decreases the ductility of the grain boundaries. By contrast, solidification cracking will not form if the eutectic liquid phases are discontinuous at the grain boundary.

The addition of filler metals is one of the most important approaches to address solidification cracking in laser-welded aluminum alloys [18–20]. Huang et al. [21] assessed the effect of different filler metal compositions on the solidification cracking of AA6xxx aluminum alloys and explained that solidification cracking was attributable to the narrow solidification temperature range and the lower eutectic temperature of the weld metal, which allow it to solidify first. The solidification crack susceptibility is a function of the welding parameters [22,23]. Schaefer et al. [24] analyzed the effects of laser welding parameters on the formation of solidification cracking. They observed that crack formation could be avoided using twin-spot optics. Cicala et al. [25] studied the influence of welding process parameters on the laser welding of an Al-Mg-Si alloy. They identified solidification cracking sensitivity as being strongly dependent on the welding travel speed and wire feed speed, given that the speed influences the solidification rate and temperature gradient. Hekmatjou et al. [4] investigated the welding parameters and preheating effect on solidification cracking behavior during pulsed laser welding and found that fast cooling rates, grain boundary separation, and heterogeneous temperature fields cause internal residual stresses in the material, which can lead to solidification cracking. They suggested that a low cooling rate and a 150 °C preheating temperature change the solidification mode from columnar to equiaxed grains and help to avoid or reduce solidification cracks. Furthermore, Friction Stir Welding (FSW) serves as a welding method for reducing solidification cracking, especially in aluminum alloys. This is achieved by its lower heat input when compared to conventional welding techniques, thereby reducing thermal stresses and associated cracking susceptibility [26].

Cracking continues to be a major challenge in the fusion welding of AA7075 alloys, particularly in laser welding. As indicated above, many studies have looked at the causes of cracking. Nevertheless, the knowledge needed to make AA7075 weldable through fusion welding is still lacking, and this welding process is yet to be fully understood. The present work aims to look at how welding parameters and different fillers affect the solidification cracking, microstructure, and mechanical properties of welded AA7075.

2. Materials and Experimental Procedure

2.1. Materials and Filler Metals

AA7075-T6 aluminum alloy (Al-Zn-Mg-Cu) with a thickness of 2 mm was used in both the Circular Patch Test (CPT) and butt joint welding configurations to investigate the hot cracking sensitivity of AA7075-T6 to shifting chemical compositions in the melting pool. The nominal chemical composition of the base material is shown in Table 1.

Table 1. Chemical composition of AA7075_T6 (wt.%).

Al	Zn	Mg	Cu	Mn	Cr	Si	Fe	Ti
Bal.	5.63	2.23	1.31	0.02	0.22	0.08	0.18	0.03

Four different filler materials, namely AA5028, AA5354, AA5356, and AA4047, were used for this study, and the chemical composition of each filler metal is presented in Table 2.

Table 2. Chemical composition of filler metals (wt.%).

Material	Al	Zn	Mg	Cu	Mn	Cr	Si	Fe	Ti
AA5028 [27]	Bal.	0.05–0.50	3.2–4.8	0.0–0.2	0.30–1.0	0.05–0.15	-	0.0–0.4	0.05–0.15
AA5354 *	Bal.	-	2.4–3.0	-	0.5–1.0	0.05–0.2	-	≤0.4	-
AA5356 [28]	Bal.	0.1	5.5	0.1	0.2	0.2	0.25	0.4	0.2
AA4047 [28]	Bal.	0.2	0.1	0.3	0.15	-	13	0.8	-

* The filler is sourced from KBM Affilips in the Netherlands, and its chemical composition is confidential.

2.2. Welding Procedure and Parameters

The welding process was executed with a pulsed TRUMPF TRUDISK 10 kW solid-state disk laser with a wavelength of 1030 nm. The laser beam focal point was set on the upper face of the welding samples. The laser beam was transmitted via a 200 µm diameter fiber to a collimating lens, resulting in focal spot diameters of 200 µm and 300 µm, respectively, at 200 mm and 300 mm distances. Table 3 and Figure 1 present the welding parameters and illustrate the schematic of the welding process.

Table 3. Welding parameters of four different filler metals.

Filler Metal	Welding Speed (m/min.)	Power (kW)	Wire Speed (m/min.)	Shield Gas	Filler Wire Angle
AA5028	1/1.5/3/4	3/3.65/6	1.5/2/4	Ar/He	40°
AA5354	1/1.5/3/4	3/3.65/6	1/1.5/2.5/4	Ar/He	40°
AA5356	1/1.5/3/4	3/3.65/8	1/2/3/4	Ar/He	40°
AA4047	1/1.5/3/4	3/3.65/8	1/1.5/2.5/6	Ar/He	40°

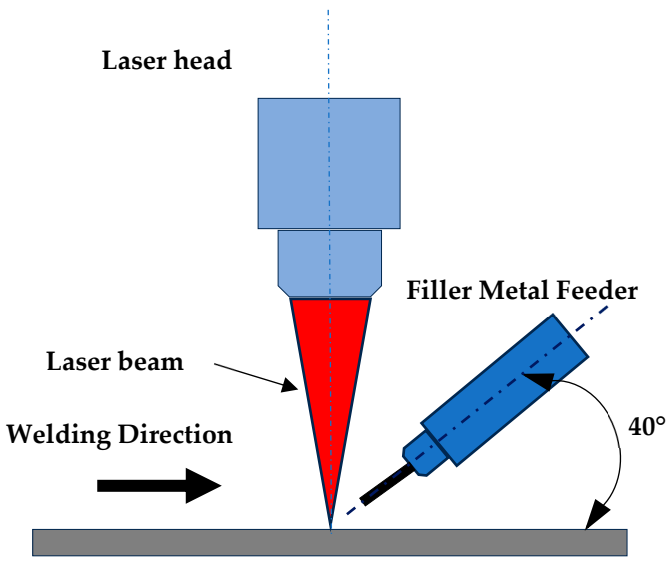

Figure 1. The schematic of the welding process.

To ensure the highest level of reproducibility for solidification cracking during welding, self-restraint was applied through specimen design and fixturing constraints using the circular patch test (CPT), as illustrated in Figure 2. In this test, the radius of the welding line path was about 19.5 mm from the center of the CPT sample. The CPT was employed to produce weld samples with varying welding parameters and different filler wire materials.

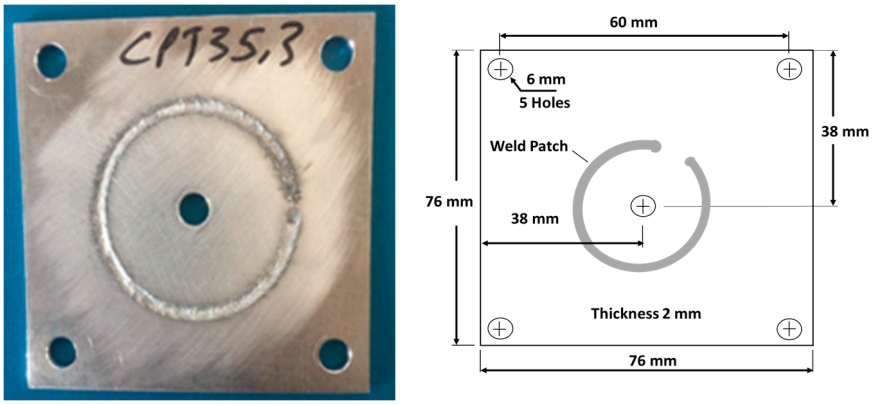

Figure 2. Configuration of CPT specimen.

2.3. X-Ray Detection of Cracks and Defects

The investigation of welds is essential for locating cracks in the fusion zone. X-ray is used as a non-destructive test (NDT) to detect surface or internal defects such as cracks or porosity. However, micro-cracks can be difficult to spot using X-ray imaging. To quantify the influence of different filler wires on solidification cracking, the cumulated crack length L_c was calculated as a measure of solidification cracking susceptibility through the following equation [24]:

$$L_c = \frac{\Sigma_i L_{c_i}}{L_{tot}} \text{ with } 0 \leq L_c \leq 1 \quad (1)$$

The length of the crack L_{c_i} was detected in the X-ray images, as shown in Figure 3. A fusion line is crack-free when $L_c = 0$, whereas $L_c = 1$ means a crack is formed in the examined weld sample.

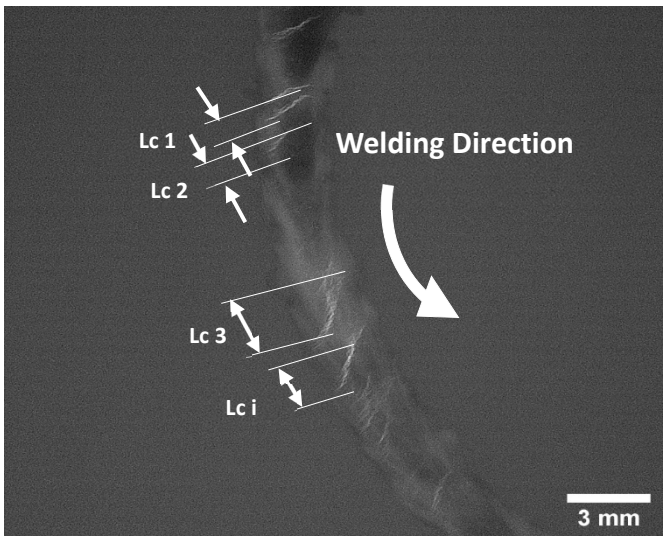

Figure 3. Calculation of cumulated crack length for the CPT sample.

2.4. Preparing Samples for Microstructure Analysis

Specimens were extracted from the area of interest in welded plates and subsequently mounted and polished for microstructure examination. Following this, the specimens were etched with Keller's reagent to reveal the dendritic structure using an etching solution (95 mL water, 2.5 mL HNO_3, 1.5 mL HC1, and 1.0 mL HF-Immerse). An optical microscope was used to characterize and investigate the microstructure. Phase analysis was performed by X-ray diffraction (XRD) using a "PANalytical X'pert Pro" X-ray diffractometer with Cu

Kα radiation. Four samples were tested for each filler metal. Vicker's microhardness test was performed, and microhardness values established the relationship between chemical composition and mechanical properties. The hardness measurements were also used to determine the size of the cracks and the degree of hardness failure [29].

2.5. The Micro-Flat Tensile Test with DIC

The specimens to be analyzed for a digital image correlation (DIC) were polished manually with 1200-grit abrasive paper. Etching was performed with Keller's reagent on the polished surface to create a fine speckled pattern to record the local deformation of tensile samples originating from the presence of defects. Local tensile specimens were equipped with an Optical High Resolution-Digital Image Correlation (OHR-DIC) device to obtain strain measurements during the test. The optical microscope was integrated with Micro-DIC to provide a comprehensive view, encompassing the specimen's 8 mm wide field area. This designated region, referred to as the "region of interest" (ROI), is where the occurrence of tensile fractures is anticipated during the deformation process. This technique provides a direct link between the microstructure map and deformation. The sample was placed under an optical microscope to capture magnified pictures of its surface. DIC was then used to process the images to obtain the rigid body displacement of the sample [30]. Four images per second were taken during the test. The spatial scale resolution used to obtain the strain field was about 4.5 µm/pixel. Image processing was carried out with OpenDIC software [31] to calculate the in-plane displacement and with ImageJ software (version 1.51) to obtain the in-plane local strain field. Micro-flat tensile tests were carried out using 5 kN tensile machines (Kammrath and Weiss GmbH, Schwerte, Germany) for the local tensile tests under crosshead velocity control. The rate at which the displacement was applied during the local tensile tests was approximately 2.5 µm per second. The local displacement was continuously recorded with a Keyence LS-7030M optical extensometer with 1µm accuracy to capture the elongation during the test. The test was also performed three times for each self-welded sample, each welded with various filler metals. Furthermore, small dog-bone specimens were extracted from CPT samples and butt joints for this test.

3. Results and Discussion

3.1. Effect of Filler Wires on Crack Reduction

Table 4 displays images of solidification crack formation within the fusion zone for both autogenous samples and samples with various filler metals, as detected through X-ray imaging. Modification of the AA7075 base material with excess magnesium (using the 5xxx series Al-Mg filler alloys) or excess silicon (using the 4xxx series Al-Si filler alloys) reduces the cracking susceptibility to acceptable levels [29,32–34]. Filler alloys AA5028, AA5354, AA5356, and AA4047 were used to weld the 7075 aluminum alloys. The effect of filler wires on the crack length L_c is illustrated in Figure 4 for both CPT and butt joint samples. The crack formation sensitivity is highest in autogenous welds, is reduced when using AA5028, AA5354, and AA4047 fillers and reaches a minimum with the AA5356 filler metal. The propensity for solidification crack formation varies with the magnesium (Mg) content, and the possibility of cracking decreases when this content is within the appropriate or optimal range [35]. This effect is most likely associated with the higher magnesium content (5.5 wt.%) in the AA5356 filler compared to other filler wires. The chemical composition was extracted to obtain an overview of the fusion zone of all the filler wires. Table 5 shows the chemical composition of the filler metals (wt.%) at the fusion zone.

Table 4. X-ray images of solidification crack formation in the fusion zone for autogenous samples and different filler metal samples.

Filler Metal	Autogenous	AA5028	AA5354	AA5356
X-ray Photos	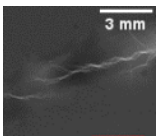	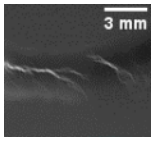	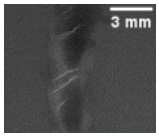	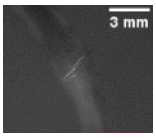

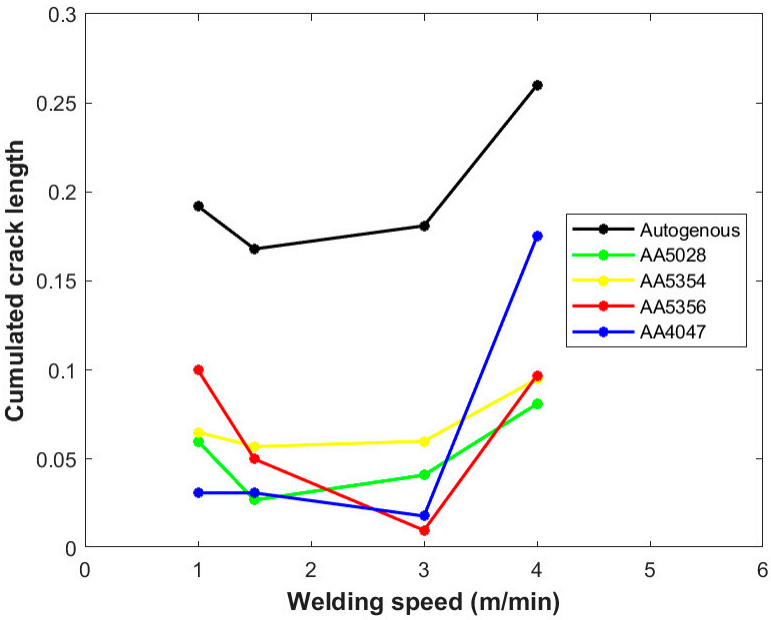

Figure 4. Effect of welding speed on cumulated crack length.

Table 5. Analysis of the overall chemical composition (wt.%) of the fusion zone with different filler wires.

Material	Al	Zn	Cu	Mg	Si	Other Elements
Autogenous	89.26	4.10	1.57	1.62	0.4	3.05
AA5028	90.96	4.04	1.11	1.39	0.01	2.49
AA5354	91.43	3.41	1.68	0.97	0.05	2.46
AA5356	90.99	3.62	1.8	1.70	0.01	1.88
AA4047	90.03	4.8	1.32	0.72	0.1	3.30

3.2. Influence of the Welding Speed on Hot Cracking

Figure 4 illustrates the effect of welding speed on the cumulated crack length (CCL). Although different fillers show different CCLs, all the fillers exhibit the same relationship between CCL and welding speed. As shown in Figure 4, the CCL is high at 1 m/min and decreases as welding speed increases until the speed reaches 3 m/min, corresponding to the lowest CCL. However, when the speed exceeds 3 m/min, the CCL increases. Figure 4 indicates that the solidification cracking tendency is lower at a 3 m/min welding speed than at other speeds. The values at this speed are roughly similar for all fillers, with the lowest seen with AA5356, and the highest with AA5354, between 0.01 and 0.06, respectively. The CCL reaches its highest levels, of about 0.26 at a 4 m/min welding speed, with autogenous laser welds. The increase in the CCL when the welding speed is raised from 3 m/min to 4 m/min, observed in both cases using different fillers and autogenous laser welds, can be attributed to insufficient liquid feeding to compensate for solidification shrinkage and thermal contraction [36].

3.3. Mechanical Properties Testing

3.3.1. Microhardness

A microhardness test was conducted, and the microhardness distributions across the transverse cross-section of laser joints are shown in Figure 5. The FZ, exposed to temperatures over 660 °C, has a low hardness average value of 85 HV. The marked drop in fusion zone microhardness, compared to the base metal and HAZ, is primarily attributed to the exceedingly rapid cooling rate during laser welding. This rapid cooling prompts the development of a fine-grained microstructure in the fusion zone, resulting in reduced microhardness. Additionally, the swift solidification in the fusion zone shortens the time available for the precipitation of strengthening elements, further contributing to the lower microhardness [37]. As shown in Figure 5, the partially melted zone (PMZ) adjacent to FZ has an average hardness value of 150 HV. The plane separates the PMZ and base metal and has an average hardness value of 146 HV, the lowest compared to the PMZ and BM. The hardness profile shows the effect of welding speed on the FZ size. The change in welding speed from 1 m/min to 4 m/min reduced the FZ width by 9%. Raising the welding speed results in a lowered heat input, which in turn causes a reduction in the FZ width.

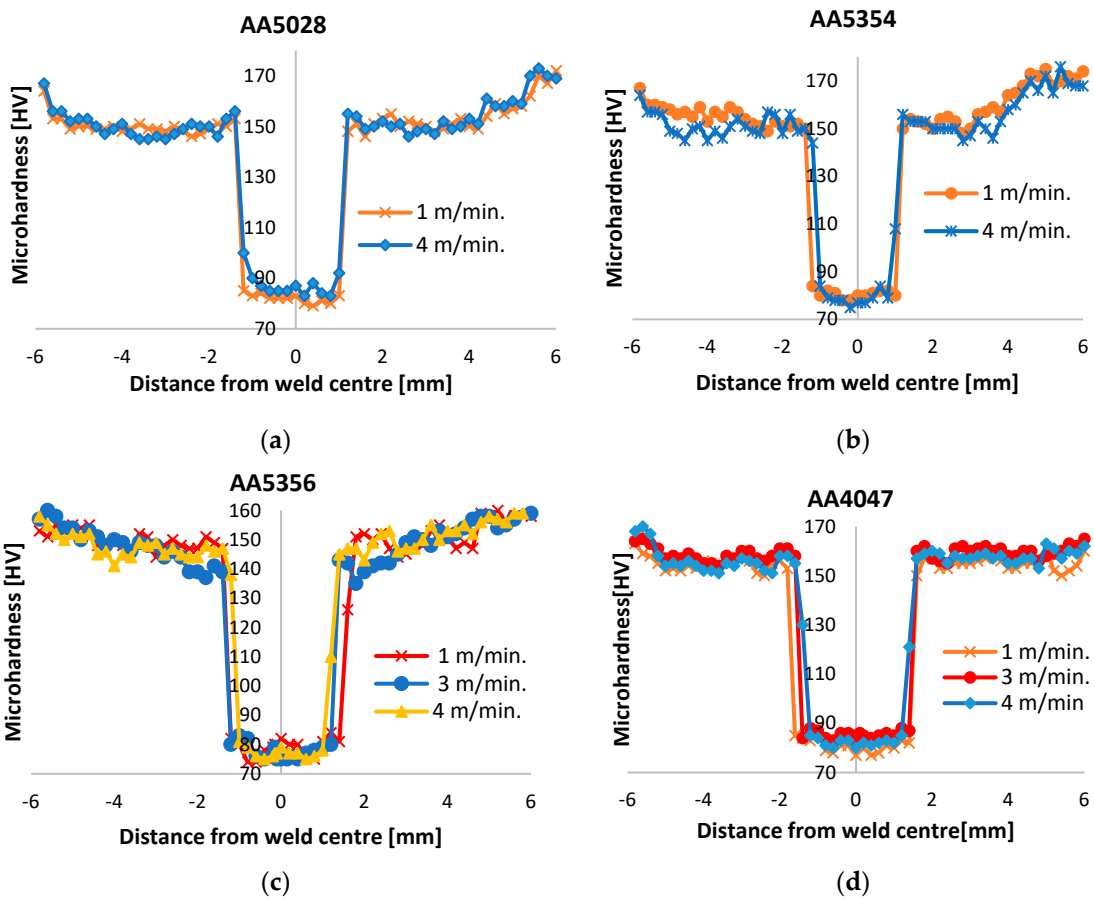

Figure 5. Microhardness test (load 100 g) results at the transverse cross-section of welds: (**a**) filler metal AA5028, (**b**) AA5354, (**c**) AA5356, and (**d**) AA4047.

3.3.2. Micro-Tensile Flat with DIC

Figure 6 compares the stress–strain experimental results for the global response of the base metal and welded samples as a function of the metal fillers. For all the samples, fracturing occurred in the plastic region of the stress–strain curves, and the fracture finally occurred in FZ. The yield strength (YS0.2) and tensile strength (TS) of samples containing the fillers AA5354, AA5028, AA5356, and AA4047 are somewhat different. The AA4047 filler exhibits superior mechanical properties, with a TS of about 353 MPa and an elongation

of 5.2%, as compared to AA5354, AA5028, and AA5356, which exhibit a TS of 227 MPa, 257 MPa, and 342 MPa and an elongation 3.15%, 3.2%, and 4%, respectively. In contrast, the sample with autogenous welds has a tensile strength of 322 MPa and an elongation of 3.8%.

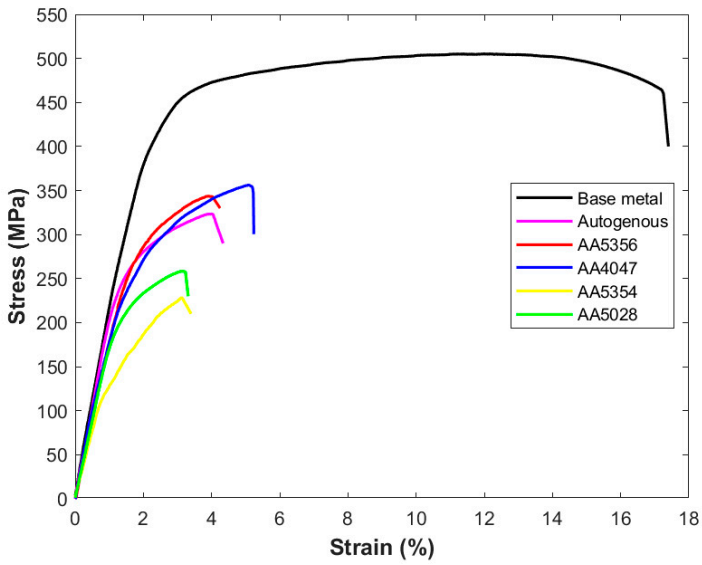

Figure 6. Stress–strain curves for samples with different fillers.

Figure 7 presents the x-direction deformation determined with the DIC of specimens A (with AA5356) and B (with AA4047). The DIC recorded strains in the longitudinal path of specimens at three stages of loading (in elastic and plastic), and the results for the two specimens are shown in Figure 7a,c. The three stages show principal stress and strain distribution across the region of interest (ROI). In the first stage, the strain was distributed uniformly across the ROI (which involved FZ and HAZ) at a stress of 257 MPa, as shown in Figure 7a. At a stress value of 288 MPa, the strain starts to localize at approximately 1.2 mm on both sides from the center of the welding line. In stage three, when the stress value reaches close to the UTS value (322 MPa), the strain begins to concentrate over the whole FZ, with a sharper concentration (and a strain value of 9%) on the left side near the interfaced line between the FZ and HAZ, with the fracture specifically situated in this location. For specimen A, the strain in the x-direction (ε_{xx}) for the ROI on both sides of the weld centerline is plotted as a function of the cross-welding direction (CWD) in Figure 7b at a stress and average strain value of 322 MPa—3.8%. Figure 7b shows the difference in strain value in the x-direction across the FZ and HAZ, where the strain value reaches 8.5% with high plane deformation.

Figure 7c shows the distribution of ε_{xx} on both sides of the weld centerline for specimen B (AA4047) in the CWD. At the first deformation stage (247 MPa—1.9%), the ε_{xx} strain fields show a strain concentration at a specific spot near the middle of the weld line. The spot discovered during the DIC test was a micro-crack that expanded until it became visible, as seen in Figure 7c. The increase in the value of the ε_{xx} strain (279 MPa—2.5%) shows the strain's spread in different regions across the FZ. For the stage before fracturing at strain level 323 MPa—3.65%, the strain begins to become more concentrated over the entire FZ, with the same distribution seen in the second stage (with a strain value of up to 5%). Despite the presence of a micro-crack near the centerline of the weld, the actual fracture took place near the interfaced line between the FZ and HAZ. This observation can be attributed to the abundant formation of the eutectic phase, which occurs excessively in both AA4047 fillers, which are rich in silicon, and AA5356 fillers, which are rich in magnesium, as indicated in Figure 8. Furthermore, the strain values ε_{xx}, as seen in Figure 7b,d, reach an average of 3.75% and 8.5% at the highest level of deformation for the AA4047 and AA5356 fillers, respectively. This finding provides additional evidence to support the

relationship between the silicon-rich AA4047 and the magnesium-rich AA5356 fillers and eutectic phase formation.

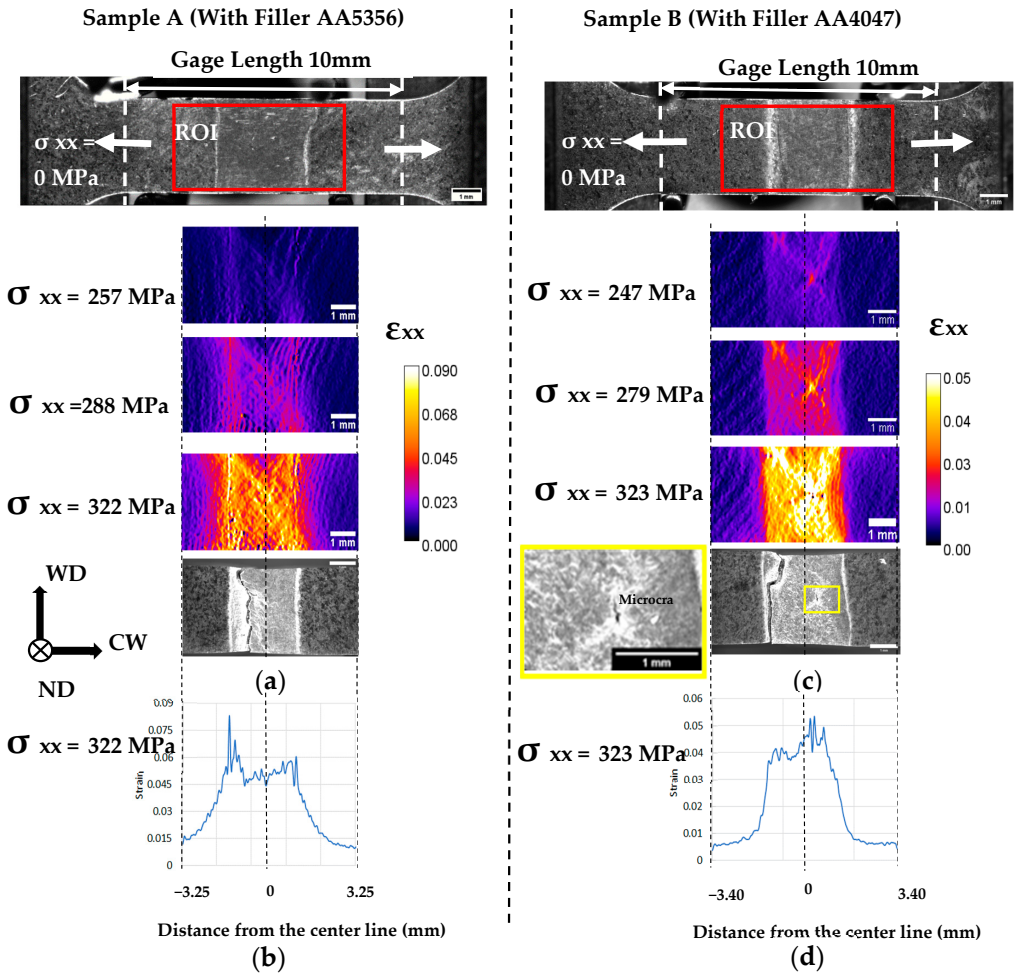

Figure 7. Local tensile field in the region of interest (red box) at various global tensile stresses for sample A (with AA5356) and sample B (with AA4047): (**a**,**c**) strain values when loading; (**b**,**d**) strain values just before fracturing.

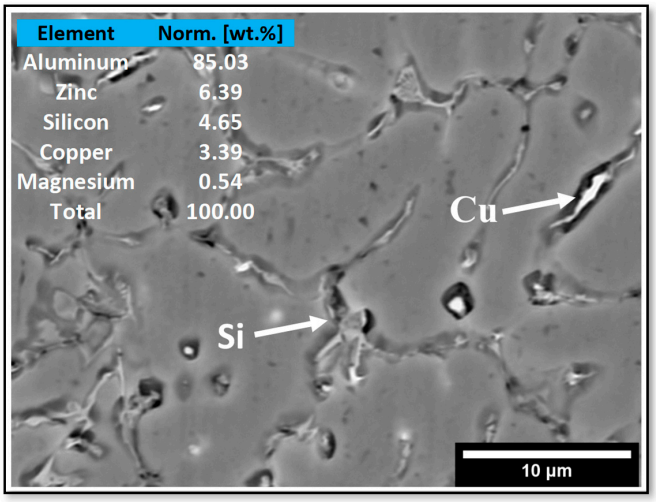

Figure 8. Precipitates rich in both Zn, Si, and Cu in a specified area in the fusion zone.

3.4. Evaluation of Microstructures

Figure 9 displays a cross-sectional view of the weld sample, which consists of an autogenous sample and one with the AA5354 filler. This image reveals the existence of defects in the fusion zone, specifically in the form of porosities. The cross-sections of the weld samples without filler were observed by optical microscopy (OM) to examine the fusion line and investigate the crack path. The macro-structure of the transverse cross-section of the bead on the plate, shown in Figure 10, indicates that there are macro-level cracks in the FZ, caused by high thermal shrinkage and strain between the low-melted eutectic phase and matrix at the final stage of solidification, which are the potential nuclei of solidification cracks produced by solidification shrinkage, gas precipitation, or vacancy supersaturation [38,39]. These cracks do not propagate to the surface of the welded sample, as shown in Figure 10. The FZ exhibits a typical dendritic structure, and some gas cavities with various magnitudes can be observed close to the welding centerline, as shown in Figure 11. These micro-voids can merge and create a micro-crack, reducing the mechanical properties of the fusion zone [40].

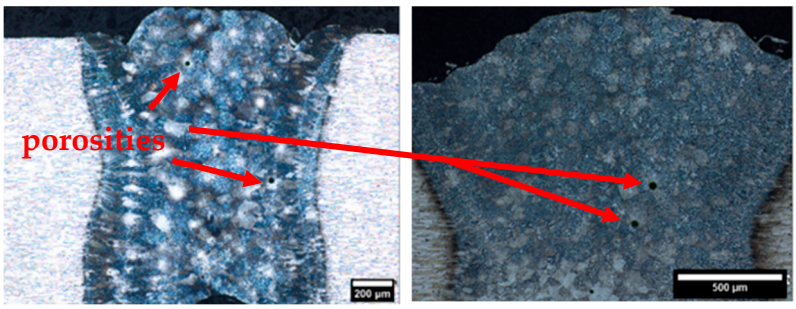

(A) (B)

Figure 9. Optical micrographs of (**A**) autogenous sample and (**B**) with AA5354 filler.

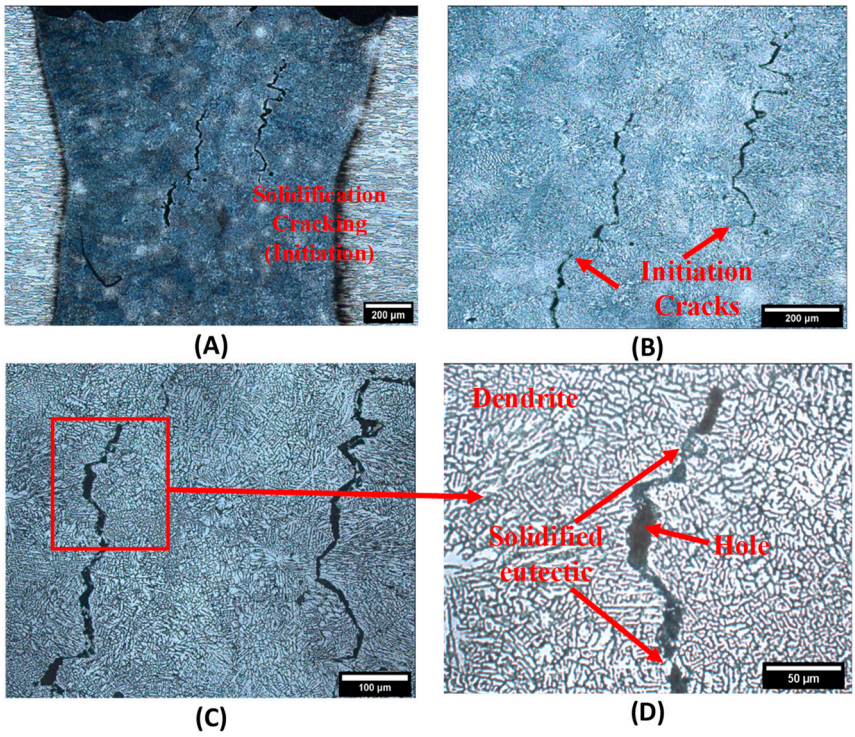

Figure 10. Initiation of solidification crack, captured at varying levels of magnification, (**A**–**C**), depicting the phenomenon under lower magnification, (**D**) offers a closer, higher-magnification view with a more precise examination of the solidification cracking.

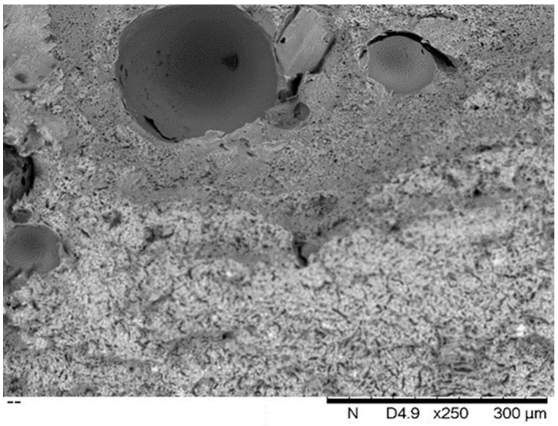

Figure 11. Shear fracture morphology along fracture path.

Figure 12 shows the grain morphology of the FZ welded with various fillers compared to the base metal. The ImageJ software was employed to identify and extract images displaying the grain boundaries, as depicted in Figure 12b, and statistical analysis was utilized to calculate the average grain size using the Linear Intercept Method (ASTM E112) [41,42]. Within the autogenous welded sample, the FZ exhibits an average grain size of 70 µm. However, when using AA5354, AA5028, AA4047, and AA5356 fillers, the average grain sizes in the FZ are 65 µm, 62 µm, 56 µm, and 53 µm, respectively. Notably, the FZs produced with these different fillers exhibit equiaxed large grain sizes, in contrast to the elongated grains with an average size of 40 µm observed in the base metal, as shown in Figure 12. The changes in grain size, resulting from the use of different fillers in comparison to autogenous welding, do not appear to significantly affect crack susceptibility or improve the mechanical properties. Figure 13 illustrates the average grain size across different welding zones for all weld fillers and autogenous welds. This analysis was conducted at specified distances, as indicated in the figure, measured from the centerline of the weld to the adjacent base metal region.

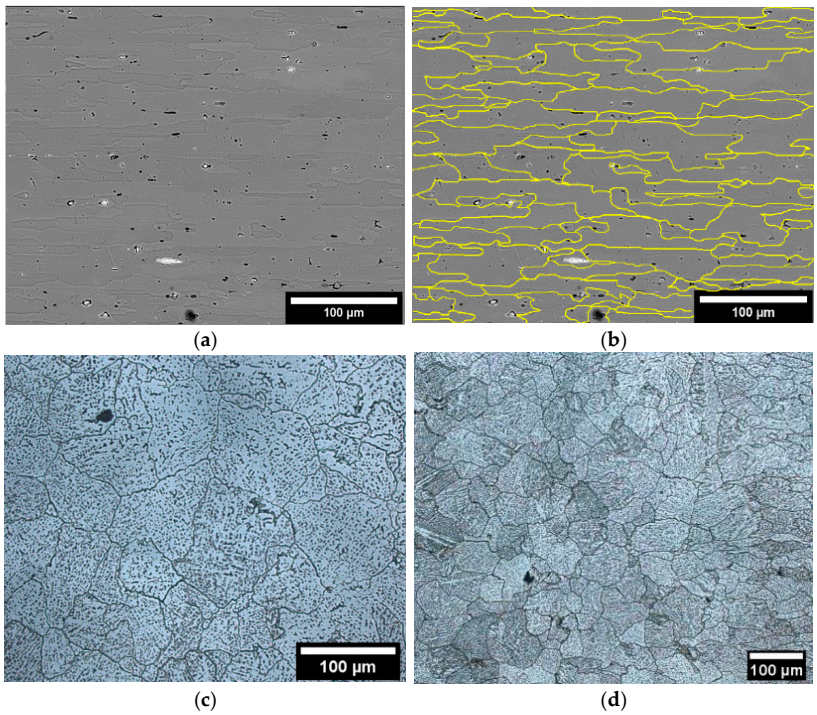

Figure 12. Microstructure images and grain size distribution of samples: (**a**) base metal, (**b**) base metal average grain size, (**c**) autogenous weld, (**d**) specimen welded with AA5356 filler.

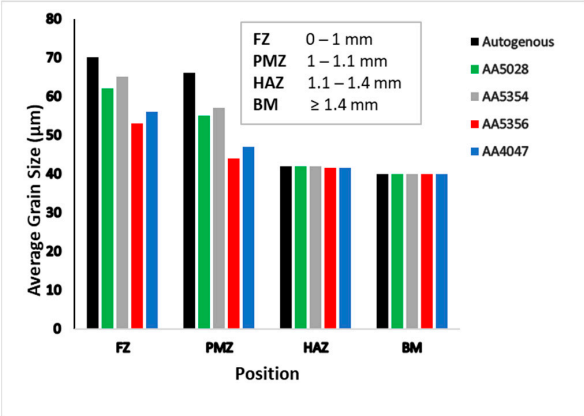

Figure 13. Illustrates the average grain size in various welding zones, including different wire fillers and autogenous welds, at a specific distance from the welding centerline.

Based on the EDS analysis, Figure 8 shows the formation of a second phase with several precipitates rich in Zn, Si, Cu, and Mg. These particles are identified to be rich in magnesium and silicon (Mg_2Si) and rich magnesium, copper, and zinc (η-phase) [10,43]. The elements were formed at various stages of solidification and were spread along the grain boundary and interdendritic regions. Figure 14 shows equiaxed large grains formed across the FZ and solidification cracks along the build direction. The observed phenomenon suggests the possibility of epitaxial grain growth, wherein nucleation takes place on previously solidified Al grains, giving rise to the formation of extensive equiaxed grains that span across multiple melt pool boundaries.

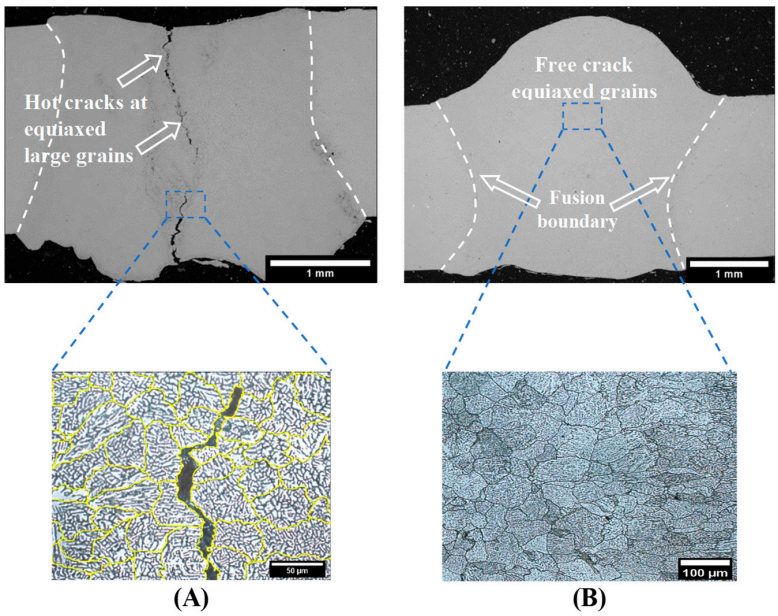

Figure 14. Variation in microstructure between autogenous and conventional fillers across the fusion line: (**A**) equiaxed large grains, (**B**) equiaxed and epitaxial grains.

The phase analysis was performed by X-ray diffraction (XRD) for four samples of each tested filler metal. Figure 15 indicates no significant difference in the phases found among the different fillers, which all showed large α-Al, Mg_2Si, and AlZn phases. Mg- and Si-rich phase precipitation confirms liquid film formation at the grain boundaries and interdendritic regions, followed by solidification and precipitation of the η-phase and Mg-Si, depending on the local Si concentration. Confirming these findings requires

further research using Electron Backscatter Diffraction (EBSD) and Transmitted Electron Microscopy (TEM) to define small-scale segregation and phase composition.

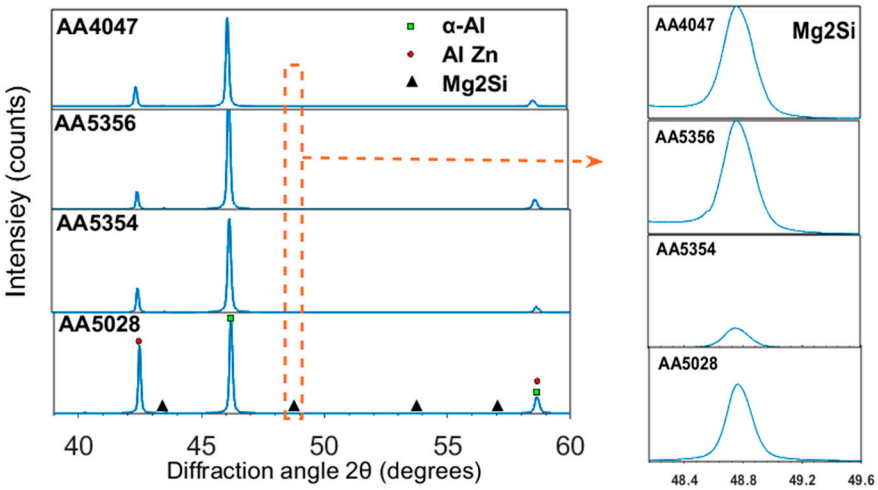

Figure 15. X-ray diffraction patterns of samples with different fillers.

4. Conclusions

In the present study, the influence of different fillers on the solidification cracking of AA7075 during the laser welding process was investigated, with the following results:

1. Crack formation sensitivity is highest in autogenous welds, reduces when using AA5028, AA5354, and AA4047 fillers, and reaches a minimum with AA5356 filler metal.
2. The solidification crack formation tendency varies with magnesium (Mg) content, decreasing when the Mg content reaches or exceeds 5.0%. This is especially evident in the AA5356 filler, characterized by its elevated magnesium content (5.5% by weight), distinguishing it from other fillers.
3. Although there are variations in the fillers that were used, they all demonstrate a consistent relationship between the CCL and the welding speed. As the welding speed increases up to 3 m/min, the CCL consistently decreases, indicating that this speed represents the optimal condition for achieving the lowest CCL across all fillers.
4. Other fillers show the lowest CCL at a 3 m/min welding speed; the lowest CCL is seen with AA5356 and the highest with AA5354, between 0.01 and 0.06, respectively. In contrast, the CCL reaches its highest level of about 0.26 with autogenous laser welds at a 4 m/min welding speed. Changing the welding speed from 1 m/min to 4 m/min reduced the width of the FZ by 9%.
5. All the samples experienced fracture within the plastic region, which ultimately occurred in the fusion zone (FZ). AA4047 and AA5365 demonstrated superior mechanical properties compared to the autogenous, AA5028, and AA5354 fillers. Throughout the DIC test, micro-cracks emerged in the FZ, which are likely attributable to the abundance of brittle (Mg_2Si) particles in this region.
6. The FZ for different fillers reveals equiaxed large grains compared to the base metal, which has an elongated grain and an average size of 40 µm. The FZ of the autogenous welded sample shows an average grain size of 70 µm, while the FZ welded with AA5354, AA5028, AA4047, and AA5356 fillers reveals average grain sizes of 65 µm, 62 µm, 56 µm, and 53 µm, respectively. These changes in grain size caused by the different fillers are not significant enough to affect crack susceptibility or enhance the mechanical properties.
7. This study is part of the research on the weldability of AA7075 using fusion welding, particularly laser welding. Further work needs to be carried out to understand the cracking phenomena in the laser welding of AA7075 in more depth. The possibility of laser welding alloy AA7075 would be a huge advantage for many industries due to the

very high welding speeds and versatility of laser welding technology in comparison to friction stir welding technology.

Author Contributions: Methodology, M.A., F.N., F.M. and X.-T.P.; Characterization, M.A.; Experimentation, F.N. and F.M.; investigation, M.A. and X.-T.P.; Analysis, M.A. and X.-T.P.; writing—original draft preparation, M.A., F.N., F.M. and X.-T.P.; writing—review and editing, M.A., F.N., F.M., T.-M.D. and X.-T.P.; supervision, T.-M.D. and X.-T.P. All authors have read and agreed to the published version of the manuscript.

Funding: This work was partially funded by NSERC (Canada), discovery grant RGPIN-2019-6574.

Data Availability Statement: Not applicable.

Conflicts of Interest: There is no conflict of interest.

References

1. Mathers, G. *The Welding of Aluminium and Its Alloys*; Woodhead Publishing: Shaxton, UK, 2002.
2. You, D.; Gao, X.; Katayama, S. Review of laser welding monitoring. *Sci. Technol. Weld. Join.* **2014**, *19*, 181–201. [CrossRef]
3. Oladimeji, O.O.; Taban, E. Trend and innovations in laser beam welding of wrought aluminum alloys. *Weld. World* **2016**, *60*, 415–457. [CrossRef]
4. Hekmatjou, H.; Naffakh-Moosavy, H. Hot cracking in pulsed Nd: YAG laser welding of AA5456. *Opt. Laser Technol.* **2018**, *103*, 22–32. [CrossRef]
5. Tomus, D.; Rometsch, P.A.; Heilmaier, M.; Wu, X. Effect of minor alloying elements on crack-formation characteristics of Hastelloy-X manufactured by selective laser melting. *Addit. Manuf.* **2017**, *16*, 65–72. [CrossRef]
6. Miyagi, M.; Wang, H.; Yoshida, R.; Kawahito, Y.; Kawakami, H.; Shoubu, T. Effect of alloy element on weld pool dynamics in laser welding of aluminum alloys. *Sci. Rep.* **2018**, *8*, 12944. [CrossRef]
7. Zykova, A.; Martyushev, N.; Skeeba, V.; Zadkov, D.; Kuzkin, A. Influence of W addition on microstructure and mechanical properties of Al-12% Si alloys. *Materials* **2019**, *12*, 981. [CrossRef]
8. Lin, R.; Wang, H.-P.; Lu, F.; Solomon, J.; Carlson, B.E. Numerical study of keyhole dynamics and keyhole-induced porosity formation in remote laser welding of Al alloys. *Int. J. Heat Mass Transf.* **2017**, *108*, 244–256. [CrossRef]
9. Stopyra, W.; Gruber, K.; Smolina, I.; Kurzynowski, T.; Kuźnicka, B. Laser powder bed fusion of AA7075 alloy: Influence of process parameters on porosity and hot cracking. *Addit. Manuf.* **2020**, *35*, 101270. [CrossRef]
10. Lin, R.; Liu, B.; Zhang, J.; Zhang, S. Microstructure evolution and properties of 7075 aluminum alloy recycled from scrap aircraft aluminum alloys. *J. Mater. Res. Technol.* **2022**, *19*, 354–367. [CrossRef]
11. Li, Q.; Xia, T.; Lan, Y.; Zhao, W.; Fan, L.; Li, P. Effect of rare earth cerium addition on the microstructure and tensile properties of hypereutectic Al–20% Si alloy. *J. Alloys Compd.* **2013**, *562*, 25–32. [CrossRef]
12. Cao, X.; Wallace, W.; Poon, C.; Immarigeon, J.-P. Research and progress in laser welding of wrought aluminum alloys. I. Laser welding processes. *Mater. Manuf. Processes* **2003**, *18*, 23–49. [CrossRef]
13. El-Batahgy, A.-M.; Klimova-Korsmik, O.; Akhmetov, A.; Turichin, G. High-Power Fiber Laser Welding of High-Strength AA7075-T6 Aluminum Alloy Welds for Mechanical Properties Research. *Materials* **2021**, *14*, 7498. [CrossRef] [PubMed]
14. Han, C.; Jiang, P.; Geng, S.; Gao, S.; Mi, G.; Wang, C. Multiphase-field simulation of grain coalescence behavior and its effects on solidification cracking susceptibility during welding of Al-Cu alloys. *Mater. Des.* **2021**, *211*, 110146. [CrossRef]
15. Zhao, P.-Z.; Liu, J.; Chi, Z.-D. Effect of Si content on laser welding performance of Al-Mn-Mg alloy. *Trans. Nonferrous Met. Soc. China* **2014**, *24*, 2208–2213. [CrossRef]
16. Balasubramanian, K.; Kesavan, D.; Balusamy, V. Studies on the effect of vibration on hot cracking and grain size in AA 7075 aluminum alloy welding. *Int. J. Eng. Sci. Technol.* **2011**, *3*.
17. Senkara, J.; Zhang, H. Cracking in spot welding aluminum alloy AA5754. *Weld. J. N. Y.* **2000**, *79*, 194-s.
18. Norouzian, M.; Elahi, M.A.; Plapper, P. A review: Suppression of the solidification cracks in the laser welding process by controlling the grain structure and chemical compositions. *J. Adv. Join. Process.* **2023**, *7*, 100139. [CrossRef]
19. Abdollahi, A.; Nganbe, M.; Kabir, A.S. On the elimination of solidification cracks in fusion welding of Al7075 by TiC-nanoparticle enhanced filler metal. *J. Manuf. Process.* **2022**, *81*, 828–836. [CrossRef]
20. Deng, A.; Chen, H.; Zhang, Y.; Liu, Y.; Yang, X.; Zhang, Z.; Zhang, B.; He, D. Prediction of the influence of welding metal composition on solidification cracking of laser welded aluminum alloy. *Mater. Today Commun.* **2023**, *35*, 105556. [CrossRef]
21. Huang, C.; Kou, S. Liquation Cracking in Full-Penetration AI-Mg-Si Welds. *Weld. J.* **2004**, *84*, s111–s122.
22. Zhang, P.; Jia, Z.; Yu, Z.; Shi, H.; Li, S.; Wu, D.; Yan, H.; Ye, X.; Chen, J.; Wang, F.; et al. A review on the effect of laser pulse shaping on the microstructure and hot cracking behavior in the welding of alloys. *Opt. Laser Technol.* **2021**, *140*, 107094. [CrossRef]
23. Kang, M.; Cheon, J.; Kam, D.H.; Kim, C. The hot cracking susceptibility subjected the laser beam oscillation welding on 6XXX aluminum alloy with a partial penetration joint. *J. Laser Appl.* **2021**, *33*, 012032. [CrossRef]
24. Schaefer, M.; Kessler, S.; Scheible, P.; Speker, N.; Harrer, T. Hot cracking during laser welding of steel: Influence of the welding parameters and prevention of cracks. In Proceedings of the High-Power Laser Materials Processing: Applications, Diagnostics,

and Systems VI, San Francisco, CA, USA, 22 February 2017; International Society for Optics and Photonics: Bellingham, DC, USA, 2017.
25. Cicală, E.; Duffet, G.; Andrzejewski, H.; Grevey, D.; Ignat, S. Hot cracking in Al–Mg–Si alloy laser welding–operating parameters and their effects. *Mater. Sci. Eng. A* **2005**, *395*, 1–9. [CrossRef]
26. Salloomi, K.N.; Hussein, F.I.; Al-Sumaidae, S.N. Temperature and stress evaluation during three different phases of friction stir welding of AA 7075-T651 alloy. *Model. Simul. Eng.* **2020**, *2020*, 3197813. [CrossRef]
27. Vorel, M.; Hinsch, S.; Konopka, M.; Scheerer, M. AlMgSc alloy 5028 status of maturation. In Proceedings of the 7th European Conference for Aeronautics and Space Sciences (Eucass), Milan, Italy, 3–6 July 2017.
28. Squillace, A.; Prisco, U. Influence of filler material on micro-and macro-mechanical behaviour of laser-beam-welded T-joint for aerospace applications. *Proc. Inst. Mech. Eng. Part L J. Mater. Des. Appl.* **2009**, *223*, 103–115. [CrossRef]
29. Kah, P.; Hiltunen, E.; Martikainen, J. Investigation of Hot Cracking in the Welding of Aluminium Alloys (6005 & 6082). In Proceedings of the 63rd Annual Assembly & International Conference of the International Institute of Welding, Istanbul, Turkey, 11–17 July 2010.
30. Pan, B.; Qian, K.; Xie, H.; Asundi, A. Two-dimensional digital image correlation for in-plane displacement and strain measurement: A review. *Meas. Sci. Technol.* **2009**, *20*, 062001. [CrossRef]
31. Vanderesse, N.; Lagacé, M.; Bridier, F.; Bocher, P. An open source software for the measurement of deformation fields by means of digital image correlation. *Microsc. Microanal.* **2013**, *19*, 820–821. [CrossRef]
32. Soysal, T.; Kou, S. Effect of filler metals on solidification cracking susceptibility of Al alloys 2024 and 6061. *J. Mater. Process. Technol.* **2019**, *266*, 421–428. [CrossRef]
33. Cao, G.; Kou, S. Predicting and reducing liquation-cracking susceptibility based on temperature vs. fraction solid. *Weld. J. N. Y.* **2006**, *85*, 9.
34. Pickin, C.; Williams, S.W.; Prangnell, P.B.; Robson, J.; Lunt, M. Control of weld composition when welding high strength aluminium alloy using the tandem process. *Sci. Technol. Weld. Join.* **2009**, *14*, 734–739. [CrossRef]
35. Kou, S. Solidification and liquation cracking issues in welding. *JOM J. Miner. Met. Mater. Soc.* **2003**, *55*, 37–42. [CrossRef]
36. Giorjao, R.; Sutton, B.; Ramirez, A. New composition based technique for solidification cracking resistance evaluation. *Metall. Mater. Trans. A* **2021**, *52*, 2512–2521. [CrossRef]
37. Perka, A.K.; John, M.; Kuruveri, U.B.; Menezes, P.L. Advanced high-strength steels for automotive applications: Arc and laser welding process, properties, and challenges. *Metals* **2022**, *12*, 1051. [CrossRef]
38. Martin, J.H.; Yahata, B.D.; Hundley, J.M.; Mayer, J.A.; Schaedler, T.A.; Pollock, T.M. 3D printing of high-strength aluminium alloys. *Nature* **2017**, *549*, 365–369. [CrossRef]
39. Coniglio, N.; Cross, C.E.; Michael, T.; Lammers, M. Defining a critical weld dilution to avoid solidification cracking in aluminum. *Weld. J.* **2008**, *87*, 237s–247s.
40. Mirakhorli, F.; Nadeau, F.; Guillemette, G. Single pass laser cold-wire welding of thick section AA6061-T6 aluminum alloy. *J. Laser Appl.* **2018**, *30*, 032421. [CrossRef]
41. Bhansali, K.; Keche, A.; Gogte, C.; Chopra, S. Effect of grain size on Hall-Petch relationship during rolling process of reinforcement bar. *Mater. Today Proc.* **2020**, *26*, 3173–3178. [CrossRef]
42. Podor, R.; Le Goff, X.; Lautru, J.; Brau, H.; Massonnet, M.; Clavier, N. SEraMic: A semi-automatic method for the segmentation of grain boundaries. *J. Eur. Ceram. Soc.* **2021**, *41*, 5349–5358. [CrossRef]
43. Kotadia, H.; Gibbons, G.; Das, A.; Howes, P. A review of Laser Powder Bed Fusion Additive Manufacturing of aluminium alloys: Microstructure and properties. *Addit. Manuf.* **2021**, *46*, 102155. [CrossRef]

Disclaimer/Publisher's Note: The statements, opinions and data contained in all publications are solely those of the individual author(s) and contributor(s) and not of MDPI and/or the editor(s). MDPI and/or the editor(s) disclaim responsibility for any injury to people or property resulting from any ideas, methods, instructions or products referred to in the content.